

0017-9310(94)00365-3

Numerical study of the compressible turbulent flow in a laser cavity

G. VLAD, O. BOIRON, G. LE PALEC and P. BOURNOT

Institut Méditerranéen de Technologie, Unité Lasers de Puissance, Technopôle de Château-Gombert,
13451 Marseille Cedex 20, France

(Received 27 June 1994 and in final form 4 November 1994)

Abstract—This paper presents a numerical study of the structure flow and heat transfer in the discharge tube of a high power CO₂ laser. A compressible turbulent model was developed in connection with simplifying assumptions. The resulting set of partial differential equations describing the flow was solved by means of the PHOENICS code. Several types of thermal boundary conditions were tested and the numerical results were found in a quite good agreement with the experimental data obtained in a previous study. The location of the reattachment point was found highly correlated with the values of the turbulent energy and the dissipation rate of turbulent energy in the entrance section. The size of the recirculation zone and the shock waves created near the exit section of the nozzle have no significant effect upon the structure flow downstream of the reattachment point.

1. INTRODUCTION

In this study, we consider the flow structure and the heat transfer in a high power CO₂ laser discharge tube. Such a flow is very complex because of compressibility, turbulence and discharge effects which interact to give the velocity and temperature field. A survey of literature shows that only a few papers deal with this problem and existing models are generally based upon very simplified assumptions. The geometry of this problem appears in Fig. 1: the gas mixture is introduced in the tube by means of a nozzle and the electric discharge is created by electrodes located at the entrance and exit section of the tube. Sonic conditions are assumed at the throat, so that the flow is compressible and turbulent.

Turbulent flow past a backward-facing step has been the subject of many works reported in the literature. Several turbulence models, such as the $k-\epsilon$ model, have been proposed. In connection with the development of numerical methods, these models were compared with experimental data in order to find their validity range. Gosman *et al.* [1] have studied several types of recirculating flows and their results are in good agreement with experimental data of Back and Roschke [2] for the case of an axisymmetric sudden expansion flow. Mace *et al.* [3] have numerically studied the case of highly compressible flows with shock waves generation. They encountered some numerical stability difficulties and their results could not be validated, but the Mach disk formation was found. In order to take the wall effects into account, Amano and Goel [4] proposed a modified Reynolds stresses turbulence model. They compared their calculations with the results given by the standard $k-\epsilon$ model for the case of an incompressible bidimensional flow. It is

difficult to choose between these models: indeed the best results (as compared with experimental data) are not obtained with the same model for the three main regions of the flow (i.e. the recirculating zone, the reattachment zone and the transition zone up to the fully developed region). Moreover, the length of the recirculating zone seems under-evaluated with the two models. Thangam and Speziale [5] also studied this problem. They found that the type of boundary conditions considered and the numerical choices such as grid size and integration field span highly affect the validity of the results. They estimated the results' validity as 12% when the turbulence is described with the $k-\epsilon$ model. An anisotropic formulation of the turbulent viscosity allows a reduction of the discrepancy between experimental and numerical results to less than 5%. For the special problem involved in the present study, Baron [6] studied the turbulent flow in a laser cavity. The electric discharge thermal effect was simulated with a constant volumetric heat source in the enthalpy equation. However, this work was undertaken with the incompressibility assumption.

It is undeniable that, in the case of a recirculating flow, discrepancies exist between $k-\epsilon$ model and experimental data. However, the associated error range is acceptable. The purpose of this paper is to study the flow structure and the heat transfer through a high power CO₂ laser discharge tube: the flow is turbulent and compressible. The first stage is to test the validity of the compressible turbulence model [7] by considering the flow without electric discharge. The electric discharge thermal effect is studied in the last part of the study. In order to solve the set of partial differential equations, we used a code based upon a finite volume formulation, PHOENICS.

etic energy (k), and the turbulent dissipation rate (ε). All these equations are expressed in the next paragraph. The pressure is deduced from the continuity equation, which itself is obtained by setting $\varphi = 1$ in equation (1). In turbulent flow problems, dependent variables are decomposed in a mean part and a turbulent part according to the Favre method [8]. PHOENICS solve mean time-averaged equations and the Boussinesq assumption allows to express the correlation between φ and velocity components. This equation can be written in the following general form :

$$\langle \rho u_i' \varphi' \rangle = -\Gamma_{t,\varphi} \overline{\text{grad } \varphi} \quad (2)$$

where φ' and u_i' are the turbulent fluctuations of φ and the velocity component along the axis x_i , respectively and $\Gamma_{t,\varphi}$ is the turbulent diffusion coefficient. For a given function (v , w , h , k or ε), the global diffusion coefficient is the sum :

$$\Gamma_\varphi = \Gamma_{l,\varphi} + \Gamma_{t,\varphi} \quad (3)$$

where $\Gamma_{l,\varphi}$ is the laminar diffusion coefficient. PHOENICS calculates Γ_φ with the following general formula :

$$\Gamma_\varphi = \rho \left(\frac{\nu_l}{\sigma_{l,\varphi}} + \frac{\nu_t}{\sigma_{t,\varphi}} \right) \quad (4)$$

where ν_l , ν_t are the kinematic viscosity of the fluid and the turbulent viscosity, respectively, $\sigma_{l,\varphi}$, $\sigma_{t,\varphi}$ being considered as laminar and turbulent Prandtl numbers for the scalar variable φ .

The standard form of the finite difference equations solved by PHOENICS for a variable is :

$$\varphi_p = \frac{\sum_{n,s,h,l} A_i \varphi_i}{\sum_{n,s,h,l} A_i} \quad (5)$$

where A_i are the links to the neighbour nodes (north, south, high and low). The compressibility effects in the transonic and supersonic regions are evaluated with the weighting factor $(1 + M^2)$ applied to the $\sum A_i$ term in the denominator of equation (5). Using this method, Davis *et al.* [9] obtained satisfactory results for Mach numbers up to 2.6. In our problem, Mach number does not exceed 1.3.

For our calculations, we used an orthogonal, 'staggered' grid. The choice of the grid density is a delicate problem. Indeed, gradients are computed by means of a first order approximation, so steep gradients require grid refinement. Also, the numerical diffusion level depends on the grid size : a coarse grid leads to some important numerical diffusion ; on the other hand, a fine grid reduces this diffusion. A preliminary study therefore will determine the influence of the grid size on the numerical results. The chosen grid has to ensure sufficient accuracy and refinements should not influence numerical results furthermore.

3. MATHEMATICAL MODEL

3.1. Equations

The flow under consideration in this study is steady, turbulent, axisymmetric and compressible. In cylindrical coordinates, with the specifications (1)–(4), the conservation equations can be written as follows :

continuity :

$$\frac{1}{r} \frac{\partial}{\partial r} (\rho r v) + \frac{\partial}{\partial z} (\rho w) = 0 \quad (6)$$

radial component of the Navier–Stokes equations :

$$\begin{aligned} \frac{1}{r} \frac{\partial}{\partial r} (\rho r v v) + \frac{\partial}{\partial z} (\rho w v) &= \frac{1}{r} \frac{\partial}{\partial r} \left[(\mu_l + \mu_t) r \frac{\partial v}{\partial r} \right] \\ &+ \frac{\partial}{\partial z} \left[(\mu_l + \mu_t) \frac{\partial v}{\partial z} \right] + S_v \end{aligned} \quad (7a)$$

$$S_v = -\frac{\partial p}{\partial r} \quad (7b)$$

axial component of the Navier–Stokes equations :

$$\begin{aligned} \frac{1}{r} \frac{\partial}{\partial r} (\rho r v w) + \frac{\partial}{\partial z} (\rho w w) &= \frac{1}{r} \frac{\partial}{\partial r} \left[(\mu_l + \mu_t) r \frac{\partial w}{\partial r} \right] \\ &+ \frac{\partial}{\partial z} \left[(\mu_l + \mu_t) \frac{\partial w}{\partial z} \right] + S_w \end{aligned} \quad (8a)$$

$$S_w = -\frac{\partial p}{\partial z} \quad (8b)$$

energy equation :

$$\begin{aligned} \frac{1}{r} \frac{\partial}{\partial r} (\rho r v h) + \frac{\partial}{\partial z} (\rho w h) &= \frac{1}{r} \frac{\partial}{\partial r} \left[\left(\frac{\mu_l}{Pr} + \frac{\mu_t}{Pr_t} \right) r \frac{\partial h}{\partial r} \right] \\ &+ \frac{\partial}{\partial z} \left[\left(\frac{\mu_l}{Pr} + \frac{\mu_t}{Pr_t} \right) \frac{\partial h}{\partial z} \right] + S_h \end{aligned} \quad (9a)$$

$$S_h = v \frac{\partial p}{\partial r} + w \frac{\partial p}{\partial z} + (\mu_l + \mu_t) \Phi. \quad (9b)$$

In equation (9b), the dissipation function, Φ , is given by :

$$\Phi = 2 \left[\left(\frac{\partial v}{\partial r} \right)^2 + \left(\frac{v}{r} \right)^2 + \left(\frac{\partial w}{\partial z} \right)^2 \right] + \left(\frac{\partial v}{\partial z} + \frac{\partial w}{\partial r} \right)^2. \quad (9c)$$

The nomenclature defines the other symbols used in the above equations. The ideal gas law allows to deduce the gas density and the temperature is calculated from the static enthalpy ($T = h/C_p$). For all calculations, the kinematic viscosity, the specific heat and the thermal conductivity are constants. It is important to note that the standard version of PHOENICS does not account for all the crossed derivatives and additional terms related to the divergence of the velocity. These ones have been introduced in a source term in order to correctly simulate the compressibility and turbulence. The electric discharge

thermal effect is simulated by means of an additional source term in the energy equation. About 80% of the total electric energy input is transformed into heat. From experimental results [10], this thermal power appears uniformly distributed in the whole volume of the discharge tube and it can be estimated as:

$$P = 8.49 \times 10^5 \text{ W m}^{-3}. \quad (10)$$

3.2. Boundary conditions

Figure 2 shows schematically the boundary conditions. We assume no-slip conditions at the walls. In case of flow without electric discharge, temperature difference between the gas and the ambient air is weak. Therefore adiabatic walls have been considered as a first approach. On the tube axis, the boundary conditions are:

$$v = 0 \quad \frac{\partial w}{\partial r} = 0 \quad \frac{\partial h}{\partial r} = 0 \quad \frac{\partial p}{\partial r} = 0. \quad (11)$$

Sonic conditions flow are assumed within the whole entrance section. The jet nozzle is treated as a fixed mass flow boundary with uniform values of all variables across the jet radius. These values correspond to the experimental ones [10]:

$$\begin{aligned} w &= 311 \text{ m s}^{-1} & v &= 0 & T &= 241 \text{ K} \\ \rho &= 0.0763 \text{ kg m}^{-3}. \end{aligned} \quad (12)$$

Exit pressure is 50 mb. The length of the discharge tube is long enough so that axial derivatives of the velocity components and enthalpy can be set equal to zero in this section. When electric discharge effects are under study, the thermal heat flux passing through the wall is not negligible. Two type of boundary conditions have been then considered: (i) the temperature is assumed constant on the wall; and (ii) a heat flux condition is prescribed.

3.2.1. *Constant wall temperature.* A dimensionless temperature is introduced [11]:

$$T^+ = \frac{T - T_p}{T^*} \quad (13)$$

with:

$$T^* = \frac{J_p}{\rho C_p U^*} \quad (14)$$

where J_p is the thermal flux which passes through the wall. The friction velocity is given by $U^* = C_\mu^{1/4} k^{1/2}$. For the viscous region, we also have:

$$T^+ = Pr y^+ \quad (15a)$$

where $y^+ = y U^*/\nu$. For the logarithmic region:

$$T^+ = Pr_t (U^+ + Pm) \quad (15b)$$

where $U^+ = U/U^*$ (U is the velocity along the wall, in the cell that is nearest from the wall) and Pm is an empirical function:

$$Pm = 9 \left(\frac{Pr}{Pr_t} - 1 \right) \left(\frac{Pr}{Pr_t} \right)^{-1/4}. \quad (16)$$

For the viscous region and the logarithmic zone, the Stanton number ($St = T^* U^*/TU$) is respectively defined as:

$$St = \frac{C_f}{2 Pr} \quad (17a)$$

$$St = \left(\frac{2 Pr_t}{C_f} + \frac{Pr_t Pm U}{C_\mu^{1/4} k^{1/2}} \right)^{-1}. \quad (17b)$$

Finally, the thermal wall heat flux is expressed as:

$$J_p = \rho C_p U St (T_p - T). \quad (18)$$

3.2.2. *Prescribed wall heat flux.* We assume that the thermal wall heat flux is:

$$J_p = H_t (T_{\text{ext}} - T_p) \quad (19)$$

where H_t is the global heat transfer coefficient. T_{ext} and T_p are the ambient temperature and the wall temperature, respectively. The mechanism involved in the heat transfer through the wall is firstly conduction and, secondly, convection and radiation between the outer wall and the ambient air. The conductive thermal resistance is approximately one hundred times less than the convective thermal resistance. It follows that H_t can be expressed as:

$$H_t = H_c + H_r \quad (20)$$

where H_c and H_r are temperature functions. They represent the convective and radiative heat transfer coefficients respectively. The radiative heat transfer coefficient is [12]:

$$H_r = \varepsilon \sigma (T_{\text{ext}} + T_p) (T_{\text{ext}}^2 + T_p^2) \quad (21a)$$

with $\sigma = 5.67 \times 10^{-8} \text{ W m}^{-2} \text{ K}^{-4}$ (Stefan-Boltzman constant) and $\varepsilon = 0.94\text{--}0.91$ (glass emissivity [14]) for $T = 290\text{--}370 \text{ K}$.

The convective heat transfer coefficient is expressed

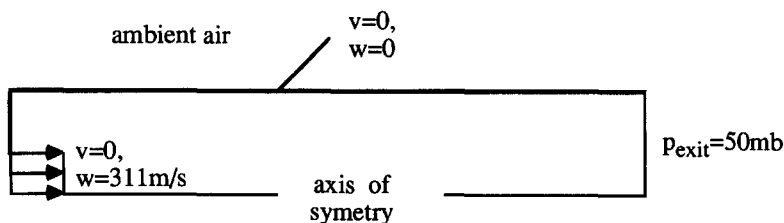


Fig. 2. Boundary conditions.

from the classical Nusselt number correlation which is valid for free convection around a horizontal cylinder :

$$H_c = \frac{\lambda Nu_d}{D} \quad (21b)$$

$$Nu_d = C(Gr_d Pr)^n \quad (21c)$$

with $\lambda = 0.0268 \text{ W m}^{-1} \text{ K}^{-1}$ (thermal conductivity of air [13]). D is the diameter of the tube, Gr_d and Pr being the Grashof and Prandtl numbers, respectively. For the range $10^4 < Ra < 10^9$, we have $C = 0.52$ and $n = 1/4$ [13].

It should be noted that in order to verify our assumptions, the thermal wall conditions were studied with several approaches. First, a very simplified model was used, which consists in computing the wall heat flux with equation (19) where T_p is the temperature of the middle of the near wall grid cell. The second approach consists to estimate the wall temperature from the wall heat balance equations (18) and (19). Finally, the last case takes the conduction process in the wall into account and the wall heat flux is determined from equation (19). In all the cases, the global heat transfer coefficient is calculated with relations (20) and (21).

4. THE TURBULENCE MODEL

The turbulence model used by PHOENICS is the k - ε model. This one is based upon a turbulent viscosity scheme. According to our assumptions, equations of the turbulent kinetic energy and the turbulent dissipation rate are :

$$\begin{aligned} \frac{1}{r} \frac{\partial}{\partial r} (\rho r v k) + \frac{\partial}{\partial z} (\rho w k) &= \frac{1}{r} \frac{\partial}{\partial r} \left[\left(\mu_t + \frac{\mu_t}{\sigma_k} \right) r \frac{\partial k}{\partial r} \right] \\ &+ \frac{\partial}{\partial z} \left[\left(\mu_t + \frac{\mu_t}{\sigma_k} \right) \frac{\partial k}{\partial z} \right] + S_k \end{aligned} \quad (22a)$$

with :

$$S_k = \mu_t \Phi - \rho \varepsilon \quad (22b)$$

$$\begin{aligned} \frac{1}{r} \frac{\partial}{\partial r} (\rho r v \varepsilon) + \frac{\partial}{\partial z} (\rho w \varepsilon) &= \frac{1}{r} \frac{\partial}{\partial r} \left[\left(\mu_t + \frac{\mu_t}{\sigma_\varepsilon} \right) r \frac{\partial \varepsilon}{\partial r} \right] \\ &+ \frac{\partial}{\partial z} \left[\left(\mu_t + \frac{\mu_t}{\sigma_\varepsilon} \right) \frac{\partial \varepsilon}{\partial z} \right] + S_\varepsilon \end{aligned} \quad (23a)$$

with :

$$S_\varepsilon = (C_{\varepsilon 1} \mu_t \Phi - \rho C_{\varepsilon 2} \varepsilon) \frac{\varepsilon}{k}. \quad (23b)$$

The turbulent viscosity is given by :

$$\mu_t = \rho C_\mu \frac{k^2}{\varepsilon}. \quad (24)$$

Additional terms due to pressure forces should appear in the k equation ($-\langle u_i' \rangle \partial P / \partial x_i, \langle p' \partial u_i' / \partial x_i \rangle$). They should also appear weighted by $C_{\varepsilon \varepsilon} / k$ in the ε equation. In order to estimate the

effects of these terms, we computed them by mean of Rubesin model [15]. In our case, we noticed no significant modifications of the results. Therefore, they will be neglected from now on.

Equations (22)–(24) are valid far away from the wall and for high turbulent Reynolds numbers ($Re_t = k^2 / \nu_t \varepsilon$). Thus, it is necessary to simulate wall friction by means of additional source terms in the momentum equations for all the cells adjacent to the wall. The coefficients C_μ , $C_{\varepsilon 1}$, $C_{\varepsilon 2}$, σ_k and σ_ε are 0.09, 1.45, 1.9, 1.4 and 1.3, respectively. For the logarithmic zone, the friction coefficient is :

$$\frac{C_f}{2} = \frac{\chi C_\mu^{1/4} k^{1/2}}{U \ln(9 C_\mu^{1/4} k^{1/2} / \nu_t)}. \quad (25)$$

This equation is valid out of the boundary layer where the flow structure is controlled by the turbulence process, that is for $y^+ > 40$. Therefore, it is important to choose the size of the mesh grid so that the calculation point next to the wall is outside the boundary layer. This condition is not valid near the reattachment point—in this last region, the following equation is used :

$$\frac{C_f}{2} = \frac{\nu_t}{yU} \quad (26)$$

which is the same as for the laminar flow case. The source term introduced in the momentum equations is :

$$S_p = -\frac{1}{2} \rho U^2 C_f. \quad (27)$$

Finally, the value of the dissipation rate of turbulent energy is determined with empirical correlations that are based upon a “mixing length” formulation. We have :

$$\varepsilon = C_\mu^{3/4} \frac{k^{3/2}}{L}. \quad (28)$$

Near the wall, the mixing length is :

$$L = \chi y. \quad (29)$$

5. RESULTS

Computations have been performed with a 35×150 grid which correctly simulate the physical phenomena. An increase in the number of cells does not lead to any significant modifications of the results. The Reynolds number for the two cases considered (with and without the electric discharge) is :

$$Re_\tau = \frac{U_0 R_0}{\nu_{1,0}} = 1.4 \times 10^4. \quad (30)$$

5.1. Flow without electric discharge

Figure 3 shows the Mach number variation near the nozzle. We see that the fluid velocity increases downstream the nozzle until the Mach number (M) is equal to 1.2. Compression waves then appear and the velocity decreases until $M = 1.1$. Downstream,

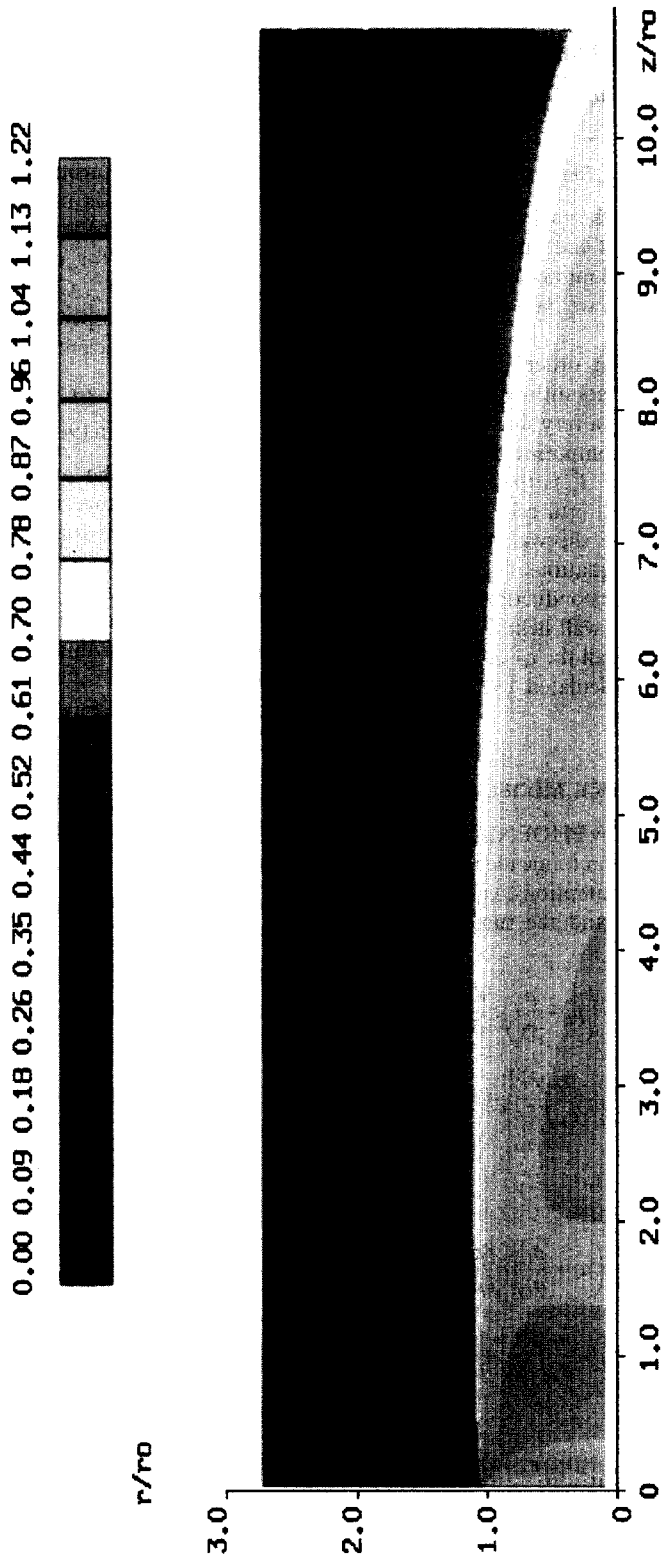


Fig. 3. Mach number variation near the nozzle.

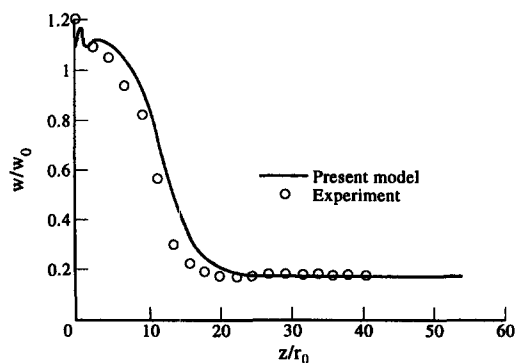


Fig. 4. Flow without electric discharge: variation of the axial component of velocity for $r/r_0 = 0$ and comparison between numerical and experimental data of [7].

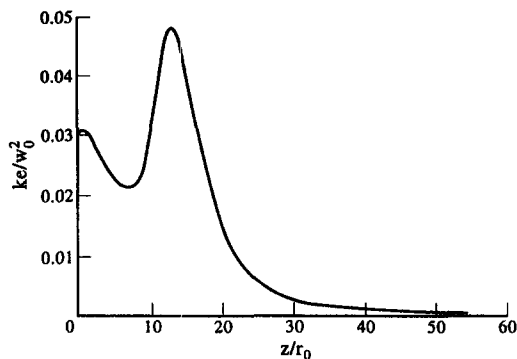


Fig. 5. Flow without electric discharge: variation of the turbulent energy for $r/r_0 = 0$.

turbulent processes become more and more important as the variation of the velocity gradient is lower and lower. Comparison between numerical results and experimental data [10] shows a good agreement, as seen from Fig. 4: the calculations correctly predict the fluid acceleration in the exit section of the nozzle. The second acceleration cannot be validated because the variation of the axial component of the velocity is too weak compared with the experimental error range. We see that the decrease in the velocity is qualitatively well described and that the reattachment point is predicted approximately 15% downstream the experimental value. The lack of experimental data did not enable us to model the turbulent characteristics in the entrance section satisfyingly. Indeed, the reattachment point location is highly correlated to the inlet values of the turbulent kinetic energy and the turbulent dissipation rate.

The axial variation of the turbulent energy (Fig. 5) shows that three regions can be distinguished: the first one is the core region ($z/r_0 < 4$), near the nozzle, where k slowly decreases. The second region is for $4 < z/r_0 < 15$: in this region the jet expands with a high decrease in the velocity and the maximal value of k is reached for $z/r_0 \approx 13$. Finally, for $z/r_0 > 15$, a boundary layer flow regime occurs with an accompanying slow diminution of k value.

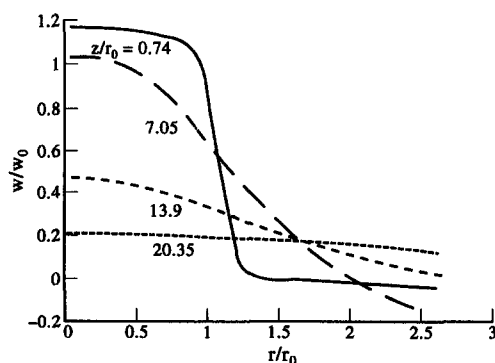


Fig. 6. Flow without electric discharge: axial velocity profiles, $z/r_0 = 0.74, 7.05, 13.9, 20.35$.

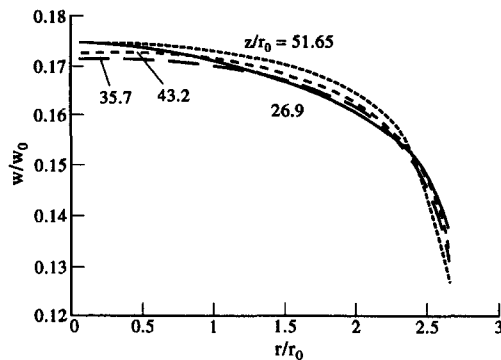


Fig. 7. Flow without electric discharge: axial velocity profiles, $z/r_0 = 26.9, 35.7, 43.2, 51.65$.

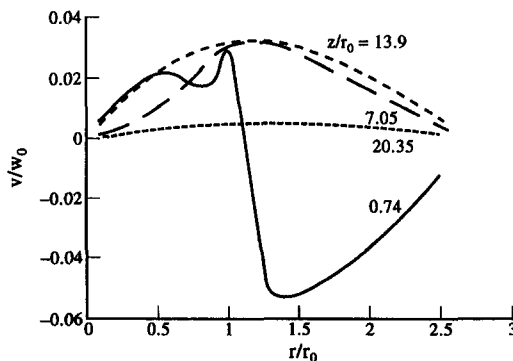


Fig. 8. Flow without electric discharge: radial velocity profiles, $z/r_0 = 0.74, 7.05, 13.9, 20.35$.

The variation of the axial velocity profiles is shown in Fig. 6 which confirms that the core rapidly vanishes and that the jet expansion induces a more flattened profile. At the discharge tube exit section, Fig. 7 shows that the flow is not fully developed. The radial velocity profiles are drawn on Figs. 8 and 9. The recirculating zone induces high values of the radial component of the velocity, which explains that the boundary layer is flattened downstream the reattachment point. In this last region, the radial component is weak and directed towards the axis of symmetry.

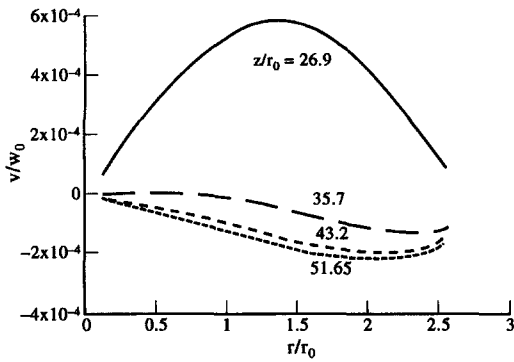


Fig. 9. Flow without electric discharge: radial velocity profiles, $z/r_0 = 26.9, 35.7, 43.2, 51.65$.

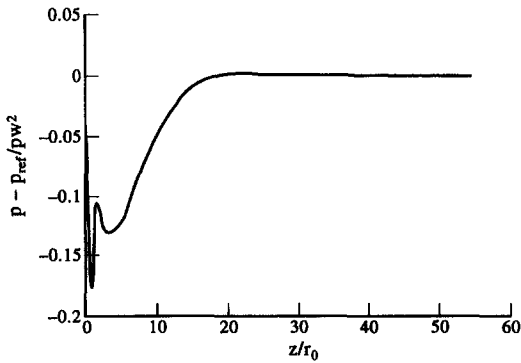


Fig. 10. Flow without electric discharge: variation of the static pressure ($r/r_0 = 0$).

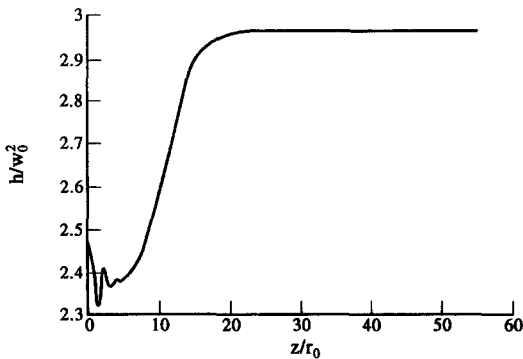


Fig. 11. Flow without electric discharge: variation of the static enthalpy ($r/r_0 = 0$).

Figure 10 shows the axial variation of the pressure and it illustrates again the succession of expansion and compression zones near the nozzle. These compression waves interact with the jet boundaries, creating expansion waves which, in turn, induce a new expansion and so on. This process vanishes and the gas compression downstream is connected with the flow deceleration.

The enthalpy variation is similar (Fig. 11): it is interesting to note the cooling effect of the gas expansion near the exit section of the nozzle. Then, due to

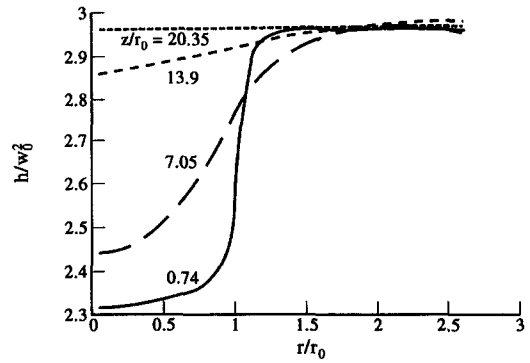


Fig. 12. Flow without electric discharge: radial variation of the static enthalpy, $z/r_0 = 0.74, 7.05, 13.9, 20.35$.

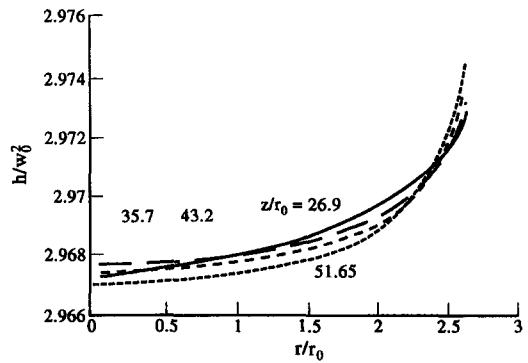


Fig. 13. Flow without electric discharge: radial variation of the static enthalpy, $z/r_0 = 26.9, 35.7, 43.2, 51.65$.

the compression wave, temperature increases. Downstream, deceleration is associated with a progressive heating effect. Radial distributions of the enthalpy are drawn on Figs. 13 and 14. The correlation between enthalpy and velocity clearly appears: near the nozzle (Fig. 12), sonic conditions occur and the enthalpy values are low compared to other regions where the Mach number is lower. In the region where the boundary layer develops (Fig. 13), the axial values of the enthalpy are lower than the wall ones.

5.2. Electric discharge thermal effects

Figures 14 and 15 illustrate the enthalpy axial variation, for the two cases of boundary conditions (constant wall temperature and wall heat flux). Near the axis of symmetry, results given by the two types of boundary conditions are very similar and they agree very well with the experimental data [10]. On the other hand, predicted wall values do not agree with the experiments, but this discrepancy is only located near the wall. The main reason is that the uniform volumic distribution of heat generated by the electric discharge assumption is not valid close to the wall. However, in order to take the real distribution of heat into account, a more complex model should be considered. A transport equation associated with each type of electric particle that interacts within the gas mixture should

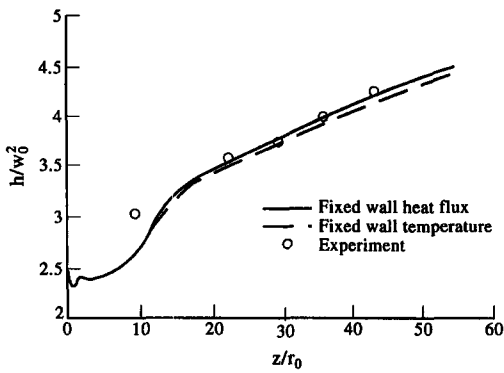


Fig. 14. Flow with electric discharge: radial variation of the static enthalpy on the axis of symmetry.

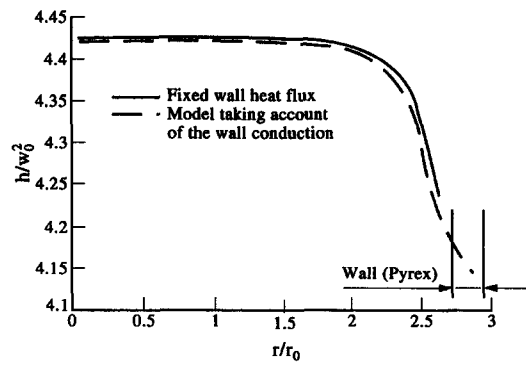


Fig. 17. Flow with electric discharge: comparison between the models with and without conduction through the wall, variation of the static enthalpy for $r/r_0 = 51.6$.

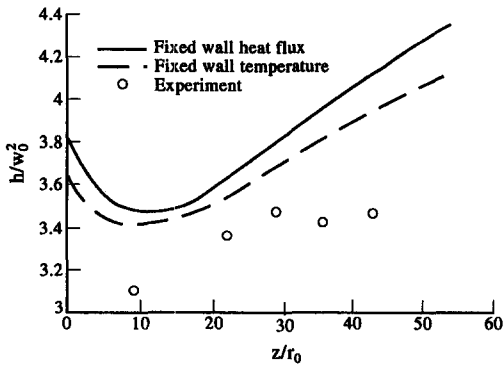


Fig. 15. Flow with electric discharge: radial variation of the static enthalpy near the wall ($r/r_0 = 0.93$).

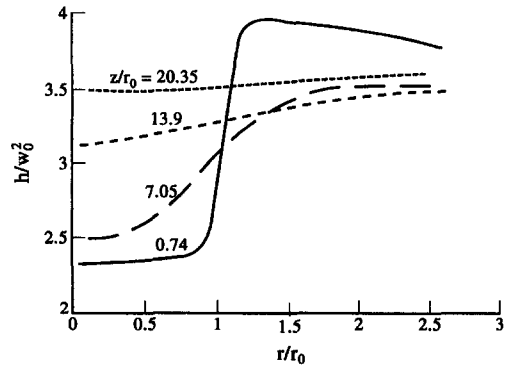


Fig. 18. Flow with electric discharge: radial variation of the static enthalpy, $z/r_0 = 0.74, 7.05, 13.9, 20.35$.

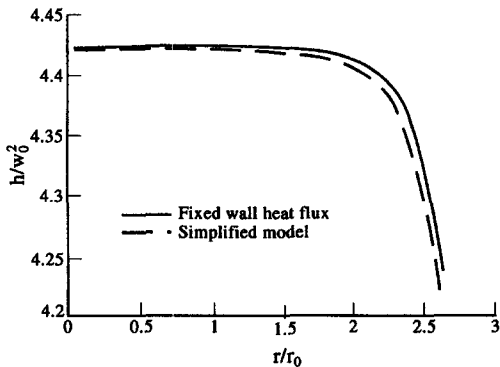


Fig. 16. Flow with electric discharge: comparison between the models that neglect the conduction through the wall, variation of the static enthalpy for $r/r_0 = 51.6$.

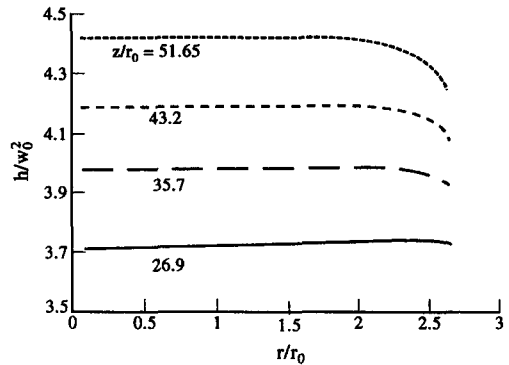


Fig. 19. Flow with electric discharge: radial variation of the static enthalpy, $z/r_0 = 26.9, 35.7, 43.2, 51.65$.

be solved with continuity, momentum, energy and turbulence equations. Moreover, in these new equations, many physical coefficients are unknown, so that such a model is not undertaken here.

As explained in Section 3, we compute several models of wall heat flux. All models lead to similar results (Figs. 16 and 17). We see that taking the conduction into account does not give significant variations of the wall temperature. This is due to the low temperature

difference between the discharge tube inner and the outer walls.

Even when the electric discharge occurs, cooling is important near the nozzle region. Figures 18 and 19 show that the radial enthalpy profile is flattened downstream of the reattachment zone according to the uniform volumic heat source assumption. Figure 19 also shows that the wall heat flux is higher at the exit section of the tube since the temperature difference between the gas and ambient air is maximal in this region. Near the entrance section, the axial velocity

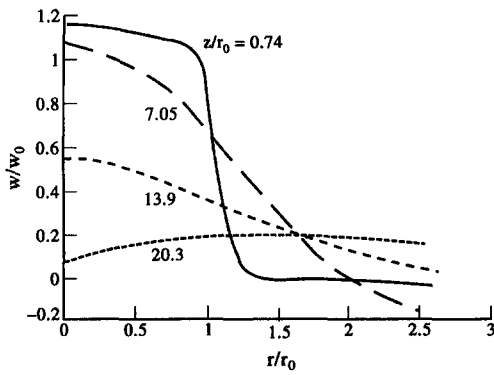


Fig. 20. Flow with electric discharge: axial velocity profiles, $z/r_0 = 0.74, 7.05, 13.9, 20.35$.

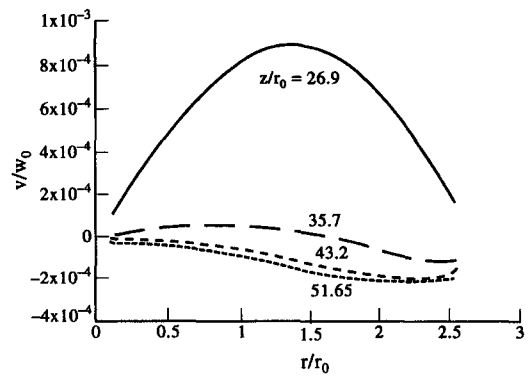


Fig. 23. Flow with electric discharge: radial velocity profiles, $z/r_0 = 26.9, 35.7, 43.2, 51.65$.

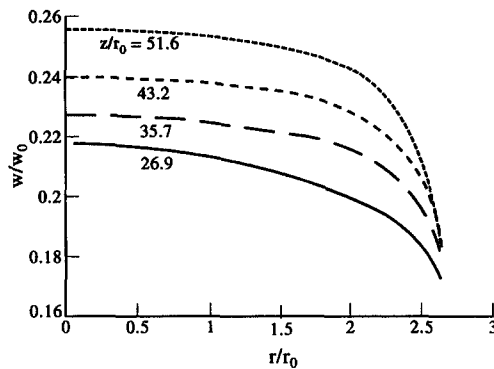


Fig. 21. Flow with electric discharge: axial velocity profiles, $z/r_0 = 26.9, 35.7, 43.2, 51.65$.

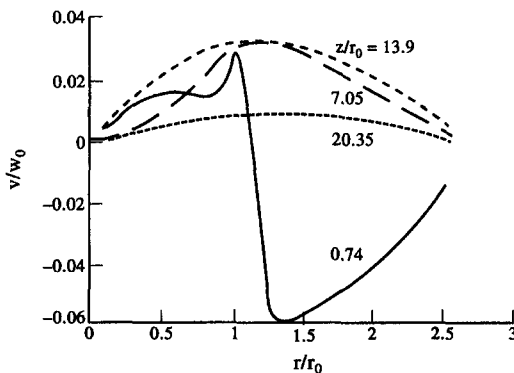


Fig. 22. Flow with electric discharge: radial velocity profiles, $z/r_0 = 0.74, 7.05, 13.9, 20.35$.

profile is similar to the profile obtained without the discharge. However, the electric discharge thermal effect becomes significant downstream and we notice the progressive acceleration of the fluid (Fig. 21). The qualitative variation of the radial component of the velocity in the recirculating zone is also similar to the previous case (i.e. without electric discharge), but values are slightly higher, as seen from Fig. 22. After

the recirculating zone (Fig. 23), the boundary layer develops and this component varies as if no discharge occurred.

From these results, we see that an electric discharge gas heating acts mainly on the axial component of the velocity. However, the flow structure remains unchanged as compared with the structure obtained without electric discharge. This means that although the heat input is great in such laser processes, convection remains forced and no transition towards mixed convection is observed.

6. CONCLUSION

In this study, a compressible turbulent model has been presented to describe momentum and heat transfer in the discharge tube of a high power CO_2 laser. For a constant Reynolds number at the entrance section, the reattachment point location is highly correlated with the inlet values of the turbulent kinetic energy and the turbulent dissipation rate. This results agree with the previous study of Thangam and Speziale [5]. The recirculation zone and the shock waves created near the nozzle have no significant effects upon the structure flow downstream of the reattachment point. Several thermal boundary conditions have also been tested and their influence upon the structure flow has been discussed. The uniform volumic heat source assumption can explain the discrepancy between predicted temperature and experimental values at the wall. The model could be improved by introducing the transport equations associated to all the particles that electrically interact in the discharge process. However some unknown coefficients appear in these equations and so the precision of the results would not be improved. Finally, it is important to note that the size of the recirculating zone is weak as compared to the total length of the discharge tube so that the proposed model correctly describes the complex flow under consideration.

REFERENCES

1. A. D. Gosman, E. E. Khalil and J. H. Whitelaw, The calculation of two-dimensional turbulent recirculation flows, *Proceedings of a Symposium on turbulent shear flows*, Pennsylvania, U.S.A. (1977).
2. L. H. Back and E. J. Roschke, Shear-layer flow regimes and wave instabilities and reattachment lengths downstream of an abrupt circular channel expansion, *J. Appl. Mech.*, 677–681 (1972).
3. A. C. H. Mace, J. S. Rogerson and A. G. Smith, Axisymmetric jet expansion into a cylindrical tube, *Proceedings of the First International PHOENICS users conference* (1985).
4. R. S. Amano and P. Goel, Computations of turbulent flow beyond backward-facing step using Reynolds-stress closure, *AIAA J.* **23**(9), 1356–1361 (1985).
5. S. Thangam and C. G. Speziale, Turbulent flow past a backward-facing step: a critical evaluation of two-equation models, *AIAA J.* **30**(5), 1314–1320 (1992).
6. F. Baron, Écoulement turbulent dans un tube à décharge. 2ème étape: Modélisation numérique de l'écoulement dans une géométrie réelle, EDF report, réf. HE44/88.29 (1988).
7. T. J. Coakley, Turbulence modelling methods for the compressible Navier–Stokes equation, AIAA 83-1693 (July 1983).
8. A. Favre, Equations statistiques des gaz turbulents. *C. r. Acad. Séanc. Paris* **246** (1958).
9. M. P. Davis, J. C. Ludwig and N. Rhodes, The application of PHOENICS to transonic jets, *Proceedings of the First International PHOENICS Users Conference* (1985).
10. O. Boiron, Caractérisation aérothermique d'un laser CO₂ de puissance à flux axial rapide. Thesis, University Aix-Marseille II, France (1992).
11. R. Shiestel, Modélisation et simulation des écoulements turbulents, *Traité des Nouvelles Technologies, série mécanique* (1993).
12. J. F. Sacadura, Initiation aux transferts thermiques, Techniques et Documentation, CAST (1978).
13. R. Giblin, Transmission de la chaleur par convection naturelle. Collection de l'Association Nationale de la Recherche Technique (1974).
14. *Handbook of Chemistry and Physics*, E-6, E-391 (66th Edn). CRC Press, Boca Raton, Florida (1985/1986).
15. M. W. Rubesin, A one-equation model of turbulence for use with the compressible Navier–Stokes equations, NASA TMX-73-128 (1976).